



LAWRENCE  
LIVERMORE  
NATIONAL  
LABORATORY

# Tent-induced perturbations on areal density of implosions at the National Ignition Facility

R. Tommasini, J. Field, B. Hammel, D. K. Bradley, O. L. Landen, R. Town, E. Dewald, S. Nagel, R. Rygg, N. Izumi

December 22, 2014

Physics of Plasmas

## **Disclaimer**

---

This document was prepared as an account of work sponsored by an agency of the United States government. Neither the United States government nor Lawrence Livermore National Security, LLC, nor any of their employees makes any warranty, expressed or implied, or assumes any legal liability or responsibility for the accuracy, completeness, or usefulness of any information, apparatus, product, or process disclosed, or represents that its use would not infringe privately owned rights. Reference herein to any specific commercial product, process, or service by trade name, trademark, manufacturer, or otherwise does not necessarily constitute or imply its endorsement, recommendation, or favoring by the United States government or Lawrence Livermore National Security, LLC. The views and opinions of authors expressed herein do not necessarily state or reflect those of the United States government or Lawrence Livermore National Security, LLC, and shall not be used for advertising or product endorsement purposes.

# Tent-induced perturbations on areal density of implosions at the National Ignition Facility

R. Tommasini<sup>i</sup>, J. Field, B. Hammel, D. Bradley, O. L. Landen, R. Town, E. Dewald, S. Nagel, R. Rygg, N. Izumi, ????

*Lawrence Livermore National Laboratory, Livermore, CA 94550*

(Dated: November 20, 2014)

Asymmetries and areal density non-uniformities seeded by time-dependent drive variations and target imperfections in Inertial Confinement Fusion (ICF) targets grow in time as the capsule implodes, with growth rates that are amplified by instabilities. Here we report on the first measurements of the perturbations on the density and areal density profiles and symmetry induced by the membranes used to hold the capsule within the hohlraum in indirect drive ICF targets. The measurements are based on the reconstruction of the ablator density profiles from 2D radiographs obtained using pinhole imaging coupled to area backlighting and as close as 150 ps to peak compression. Our study shows, for the first time, a clear correlation between the modulations imposed on the areal density and the reduced measured neutron yield, and a 3x reduction in the areal density perturbations when a high-adiabat pulse shape is used as opposed to the low-adiabat pulse-shape.

## **Keywords:**

**PACS:** 52.57.-z, 52.57.Fg, 87.59.-e

## **I. INTRODUCTION**

Implosion efficiency depends on keeping the in-flight ablator and fuel as close as possible to spherical at all times while maintaining the required implosion velocity and in-flight aspect ratio. Asymmetries and areal density non-uniformities seeded by time-dependent drive variations and target imperfections grow in time as the capsule implodes, with growth rates that are amplified by instabilities. One way to diagnose them is by imaging the self-emission from the implosion core. However this technique, besides only providing direct information of the shape of the hot emission region at final assembly, presents complications due to competition between emission gradients and reabsorption. Time resolved radiographic imaging, being insensitive to this effect, is therefore an important tool for diagnosing the ablator and the shell in inertial confinement fusion (ICF) implosions. Here we report on the first measurements of the perturbations on the areal density profiles and symmetry induced by the membranes used to hold the capsule within the hohlraum in indirect drive ICF targets. The measurements are based on the reconstruction of the ablator density profiles from 2D radiographs obtained using pinhole imaging coupled to area backlighting and as close as 150 ps to peak compression. Our study shows for the first time a clear correlation between the modulations imposed on the areal density and the measured neutron yield.

## **II. EXPERIMENT DESCRIPTION**

The measurements here reported are derived from the analysis of 2D x-ray radiographs [1] produced by a backlighting technique that has been developed to image the imploding ablator in-flight down to a radius of about 150  $\mu\text{m}$ . In a variant of a typical indirect drive [2,3] experimental setup, 2 quads of the NIF are used to drive an area backlighter foil, located 12 mm from the capsule center, in the equatorial plane. The remaining 184 laser beams illuminate the inner of a gold hohlraum that reemits the laser energy into a blackbody X-ray spectrum. Part of the X-rays are absorbed by the outer layer of the capsule, located at the center of the hohlraum, which is ablated and therefore generates a spherically-symmetric rocket reaction that compresses the capsule. The radiographs of the imploding capsule, viewed along an equatorial (i.e. perpendicular to the hohlraum axis) line of sight, are imaged by an array of pinholes,  $\sim 15\mu\text{m}$  in diameter, and recorded on a gated X-ray detector [4], through a clear, unobstructed, sight provided by two  $800\times 800\mu\text{m}$  diagnostic patches on the opposite sides of the hohlraum walls. Since each pinhole relays a radiograph at a different location on the gated detector, we can record radiographs spaced by 40-50ps and covering a time interval of about 400-500ps.

TABLE I. Main Laser, capsule, and hohlraum parameters for each shot, along with the thickness of the membrane supporting the capsule inside the hohlraum

Shot #	Laser			Capsule		Hohlraum			Tent
	Pulse Shape	Energy MJ	Peak Power TW	Abl Thk $\mu\text{m}$	Outer Radius $\mu\text{m}$	LEH Diam mm	Inner Length mm	Inner Diam mm	thickness $\mu\text{m}$
N130411	Low-Foot	1.33	356	210.7	1142.4	3.102	9.436	5.75	0 <sup>(1)</sup>
N130630	Low-Foot	1.36	367	207.8	1137.6	3.373	10.130	5.75	15
N121219	Low-Foot	1.34	345	209.4	1129.5	3.102	9.126	5.75	45
N121218	Low-Foot	1.34	363	209.3	1132.9	3.102	9.711	5.75	48
N121210	Low-Foot	1.33	360	209.8	1119.2	3.101	9.425	5.75	110
N121202	Low-Foot	1.33	365	207.8	1110.6	3.101	9.429	5.75	110
N130808	High-Foot	1.33	362	206.9	1128.0	3.373	10.130	5.75	15
N130508	High-Foot	1.33	367	207.4	1140.8	3.373	10.127	5.75	45
N130303	High-Foot	1.31	337	207.4	1106.7	3.102	9.433	5.75	110

(1) capsule held in place by stalk

For the experiments of interest here, 35-60kJ of energy from the 8 NIF backlighter laser beams were focused on a Ge foil, delivering up to 18 TW at an irradiance of  $1\text{-}3 \times 10^{15} \text{ W/cm}^2$ , and exciting the He-like 2-1 resonance lines at  $\sim 10.2 \text{ keV}$ , with about 1% efficiency. The targets consist of a 5.75 mm inner-diameter gold hohlraum having lengths ranging from 9.126mm to 10.130mm. A plastic shell,  $\sim 2.3 \text{ mm}$  diameter, (graded Si-doped with the stair-stepped 1%, 2%, 1% graded layered distribution [5]), with thickness varying from  $206.9 \mu\text{m}$  to  $210.7 \mu\text{m}$ , is placed at the center of the hohlraum and filled with  $\sim 6.7 \text{ mg/cm}^3$  of 30/70 mixture of D-3He gas. The hohlraum is driven with either a 21-ns-long, 4-shock Low-Foot pulse[6], or a 15-ns-long, 3-shock High-Foot pulse[7], with energy ranging between 1.31MJ and 1.36MJ and power ranging between 337TW and 367TW. The capsules are held in place by means by two thin plastic membranes (tents), with thicknesses between 15nm and 110nm. In one case (shot N120411) a stalk replaced the tent. The detailed values of the main experimental parameters for each shot are shown in Table 1.

### III. DENSITY RECONSTRUCTION FROM RADIOGRAPHS AND ANALYSIS METHOD

Prior to the reconstruction of the ablator from the transmission radiographs, these are corrected for backgrounds and backlighter non-uniformities using a recently developed technique that takes advantage of the parallax [8] from the different pinholes. This procedure can

also be used to increase the signal-to-noise ratio, by combining radiographs from different pinholes.

The ablator density is calculated from the 2D radiographs using both a forward iterative unfolding procedure, the details of which will be discussed in a separate article, and a direct Abel inversion [9]. The first approach has the advantage of avoiding data deconvolution to remove spatial blurring due to the pinholes, temporal blurring due to the camera temporal resolution, and the effect of the two-dimensional camera point spread function, as these diagnostic characteristics can be part of the forward unfolding procedure. In the second case the data has to be deconvolved of any blur prior to undergo through the Abel inversion procedure. [5] Both methods allow left-right asymmetry in the reconstructed density profile, in the first case by including the asymmetry in the forward-propagated functions, in the second by using left-right tapered density profiles. [9] Once the ablator density  $\rho(r, \theta)$  is reconstructed, the areal density, defined as

$$\rho R(\theta) = \int_0^R \rho(r, \theta) dr \quad (1)$$

is calculated by numerical integration along the radial coordinate for each angle. The perturbations in areal density are characterized by the fractional amplitude  $\Delta(\rho R)/\Delta \rho R$  of the ripples in  $\rho R$ .

This analysis method has been validated against simulations (B. Hammel, HYDRA):  $\Delta(\rho R)/\Delta \rho R$  values calculated after the reconstruction of the density from synthetic radiographs of simulated implosions of different capsules match the values from simulations within 3%

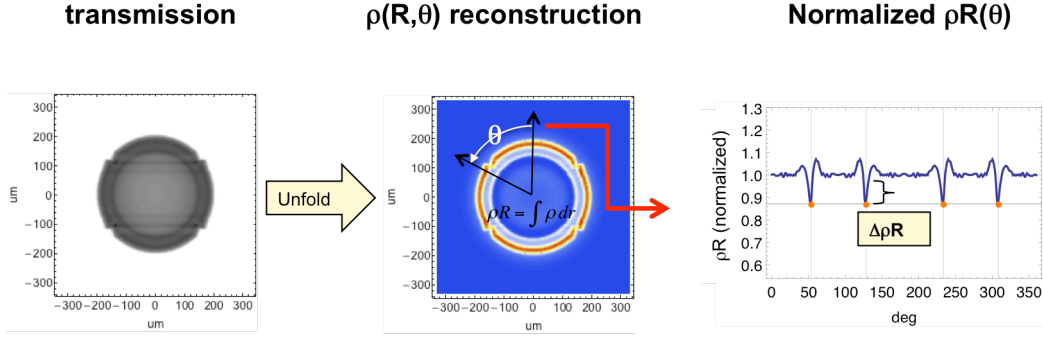


FIG.1. Analysis procedure applied to a simulated implosion of a capsule with 50nm-thick supporting tent. Left: Simulated radiograph. Center: capsule density,  $\rho$ , reconstruction based on unfolding code. Right: The areal density is calculated by numerical integration along the radial coordinate. The fluctuations in areal density are characterized by the fractional amplitude  $\Delta(\rho R)/\rho R$  of the perturbations in  $\rho R$ . On experimental data the fractional amplitudes are averaged over the 4-locations, one on each quadrant.

under a wide range of tent parameters. The analysis method is illustrated in Fig. 1.

#### IV. RESULTS: LOW-FOOT PULSE SHAPE

Figure 2.a shows the radiograph from shot N121210, at a time corresponding to  $\sim 630$ ps prior to bang time. In this particular case a  $110\mu\text{m}$ -thick tent was used. Two horizontal and almost parallel features are visible across the radiographs at positions corresponding to about  $+180\mu\text{m}$  and  $-180\mu\text{m}$  on the vertical axis. We proved that the tent

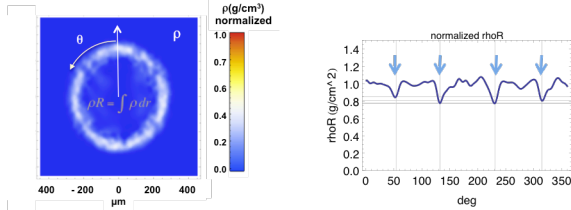


FIG.3. Left: shell density,  $\rho$ , reconstruction from radiograph of imploding capsule supported by 110nm-thick tent (N121210). Right: normalized areal density with clear 4-fold perturbations seeded by the tent.

induces these features on the radiographs by comparing with stalk mounted capsule implosions. Figure 2.b shows the radiograph from shot N130411, at a similar radius for the imploding shell as in N121210 and with similar other shot parameters. In this case the tent was not used, as the capsule was held at hohlraum center by means of a stalk, and no horizontal features can be seen. The implications of tent features on radiographs and radiographs shape are further discussed in Ref. [10]. As a general comment the radiographs from shots using a tent show perturbations persistent across the implosion. Such perturbations are not

visible in shots where no tent was used and are less visible in shots using thinner tents.

Figure 3.a shows the normalized density reconstruction for N121210. The features induced by the 110nm-thick tent

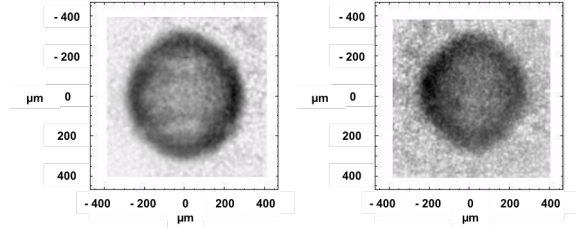


FIG.2. Comparison of radiographs of imploding capsules supported by tent (Left) and by stalk (Right). No tent-induced perturbations are seen in the second case.

on the radiographs are clearly unfolded in a ring-like pattern that results in the rather sharp 4-fold perturbations in the reconstructed density at  $\sim 45$ deg in each of the four quadrants. The areal density  $\rho R$  is then calculated by numerical integration along the radial coordinate according to the definition in Equation (1) and for each radiograph. At this point it is convenient to normalize the areal density: by doing this, and since the areal density does not depend on the radial coordinate, we can average the areal density using radiographs from different pinholes, thereby increasing the signal to noise and emphasizing the areal density asymmetries that are persistent along the ablator trajectory. The result of this procedure is shown in Figure 3b, for N121210 and shows clear 4-fold perturbations in the  $\rho R$  profile. In this particular case, a 110nm-thick tent was used and a fractional  $\Delta(\rho R)/\rho R = 19 \pm 2\%$  was measured, for an average center of mass radius of the ablator of  $250\mu\text{m}$ . In figure 4 we summarize the results obtained by

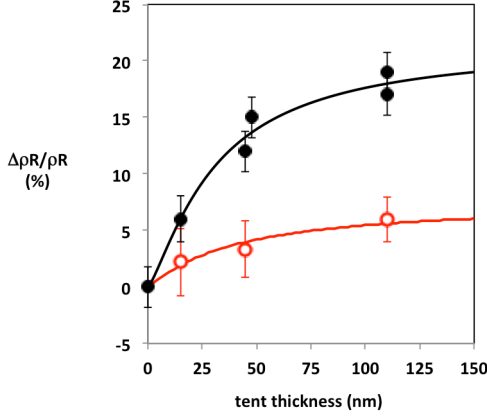


FIG.4. The fractional amplitude variation of the areal density versus tent thickness shows increases with increasing tent thickness. Closed circles = Low-Foot pulse shape; Open circles = High-Foot pulse shape.

applying this analysis to the experiments listed in Table 1. The amplitude of perturbations observed in the frame-averaged  $\rho R$  profiles increases with increasing tent thickness and scales as

$$\Delta(\rho R)/\rho R \sim 1/(1 + d^{-\alpha}) \quad (2)$$

where  $d=t/t_c$ , i.e. the tent thickness,  $t$ , normalized by a characteristic value  $t_c$ , and the specific values of the parameter  $t_c$ , and the exponent  $\alpha$ , depend on the implosion parameters, e.g. pulse shape, and might depend on the residual corrections due to the experimental conditions, e.g. effective radiograph resolution, signal/noise ratio.

The meaning of the characteristic thickness  $t_c$  is clear from the scaling shown in equation (2): it represents the thickness at which the fractional amplitude variations in the areal density reach half of the asymptotic value of the function at right hand side of eq.(2). For  $t < t_c$  the growth of the fractional amplitude variations scales nearly linear with the thickness of the tent.

In the case of the experiments in Table 1, driven by Low-Foot pulse shape and reported in Fig.4 by closed circles,  $t_c = (30 \pm 2) \mu\text{m}$ ,  $\alpha = 1.3$ .

## V. RESULTS: HIGH-FOOT PULSE SHAPE

A general relationship can be derived linking the fractional variations in areal density to the convergence ratio,  $C_r = R_i/R_f$ , of an implosion:

$$\frac{\Delta(\rho R)}{\rho R} = 2 \frac{\Delta U}{U} c_r \quad (3)$$

where  $U$  is the average implosion velocity,  $c_r = (R_i - R_f)/R_f = C_r - 1$  is the differential convergence ratio,  $R_i$  and  $R_f$  are the initial and final radii of the shell, respectively. Eq (3) shows that the areal density non-uniformities are amplified according to the differential convergence ratio and lower degrees of non-uniformity amplification are expected for implosions having lower convergence.

Indirect drive implosions driven by a high-adiabat, or High-Foot, pulse shape have recently achieved gains close to unity on the NIF [7,11]. These pulses are designed to enhance the hydrodynamic stability of the shell by delivering higher initial radiation temperature in the “foot” of the pulse, thereby setting the imploding shell on a higher adiabat, increasing the ablation rate and density scale lengths in the shell [12,13]. Both effects contribute to reduce the Rayleigh-Taylor instability growth rates of the shell perturbations, including those induced by the tent. Moreover, because of the initially greater shock strength, the first shock transits the shell more quickly and the overall pulse is shortened at the expense of shell convergence ratio, from a value of  $\sim 40$  down to  $\sim 30$  for the Low-Foot and High-Foot pulse, respectively. This in turn also contributes to a lower amplification of the areal density non-uniformities, as described by equation (3). Figure-5. Left shows the simulated transmission radiographs of two implosions having the same parameters, including a 50nm thick tent, but driven a Low-Foot and a High-Foot pulse shape. The density reconstruction, following the unfold procedure, is shown in Figure-5.Center, emphasizing the reduced growth of the tent-induced perturbations in the High-Foot case. From the normalized  $\rho R$  profiles, reported in Figure-5.Right, we measure a 3x reduction in the  $\Delta(\rho R)/\Delta \rho R$  when the High-Foot pulse is used.

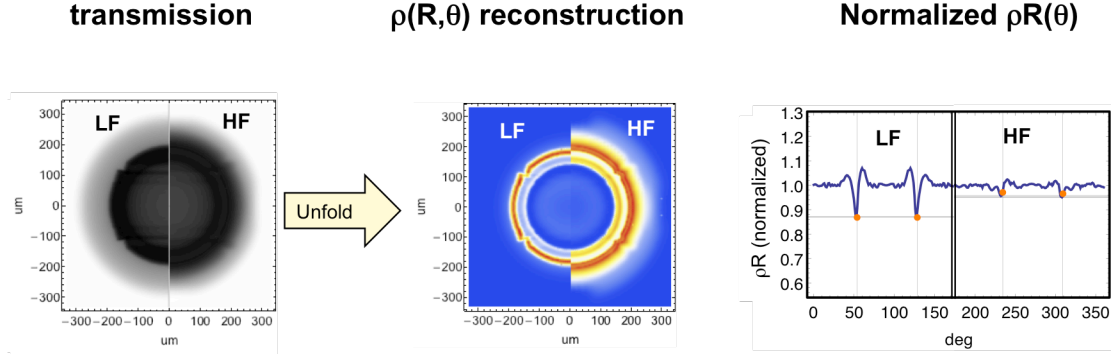


FIG.5. Analysis procedure applied to simulated implosions of capsules with 50nm-thick supporting tent and driven by a Low-Foot (LF) and a High-Foot (HF) pulse. Left: Simulated radiographs. Center: reconstructed capsule densities. Right: The fluctuations in the areal density show a 3x reduction when the High-Foot pulse is used.

Figure 6 shows a comparison of radiographs from Low-Foot (left) and High-Foot (right) pulse driven implosions. In this case the tent thickness was 47nm and 45nm, respectively, and while still noticeable, the tent feature on the radiograph is noticeably reduced in the High-Foot case.

For a quantitative comparison, the three implosions listed in Table 1 and driven by the High-Foot pulse shape have been radiographed and analyzed according to the procedure described earlier. The measured  $\Delta(\rho R)/\Delta\rho R$  are shown in Figure 4, where the measurements for High-Foot implosions are represented by open circles and are compared to the ones from Low-Foot implosions, represented by closed circles. For the High-Foot pulse, the amplitude of perturbations observed in the frame-averaged  $\rho R$  profiles also increases with increasing tent thickness, but at a slower rate, with a reduced scaling exponent  $\alpha \sim 1$ , and an increased characteristic thickness  $t_c = (40 \pm 4) \mu\text{m}$ . We

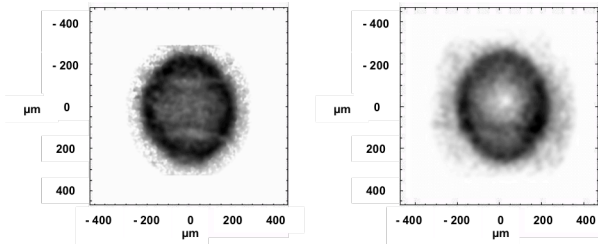


FIG.6. The comparison of radiographs from Low-Foot (left) and High-Foot (right) pulse driven implosions of capsules using 47nm- and 45nm-thick tent, respectively, show dramatic reduction of the features in the radiographs in the High-Foot case.

also note that the average reduction in  $\Delta(\rho R)/\Delta\rho R$ , calculated by the ratio of the two scaling fits amounts to a

factor of 3.2, while the ratio of the asymptotic values is 2.9. Both are close to the simulated cases discussed above.

## VI. RESULTS: IMPACT ON NEUTRON YIELD

In order to correlate the areal density non-uniformities with capsule performance, Figure 7 reports the measured (DD) neutron yield over expected yield ratio vs the fractional amplitude  $\Delta(\rho R)/\Delta\rho R$ , for the Low-Foot driven implosions. The measured over expected yield ratio drops as the  $\rho R$  perturbations induced by tent increase. The plot shows a reduction in yield performance approaching factors of about 2x when the induced fractional perturbation  $\Delta(\rho R)/\Delta\rho R$  reaches the 20% value, i.e. for tent thicknesses in the 110nm range. This is consistent with the areal density asymmetry limiting the compression and breaking up the shell relatively early in its trajectory, thereby significantly reducing the conversion of implosion kinetic energy to hot spot internal energy and limiting the produced neutron yield in the experiments. [14]

## VII. CONCLUSIONS

We have reported on the first measurements of the perturbations on the density and areal density profiles and symmetry induced by the membranes used to hold the capsule within the hohlraum in indirect drive ICF targets. The measurements are based on the reconstruction of the ablator density profiles from 2D radiographs obtained using pinhole imaging coupled to area backlighting and as close as 150 ps to peak compression.

The areal density perturbations increase with increasing tent thickness in both Low- and High-Foot cases, but are reduced by a factor of  $\sim 3.2$  when the later pulse-shape is used. Our study shows, for the first time, a clear correlation between the modulations imposed on the areal density and the reduced measured neutron yield.

## ACKNOWLEDGMENTS

This work performed under the auspices of the U. S. Department of Energy by Lawrence Livermore National Laboratory under Contract No. DE-AC52-07NA27344 and by Los Alamos National Laboratory under Contract No. DE-AC52-06NA25396.

## REFERENCES

- [1] J. R. Rygg, O. S. Jones, J. E. Field, M. A. Barrios, L. R. Benedetti, G. W. Collins, D. C. Eder, M. J. Edwards, J. L. Kline, J. J. Kroll, O. L. Landen, T. Ma, A. Pak, J. L. Peterson, K. Raman, R. P. J. Town, and D. K. Bradley, *Phys Rev Lett* **112**, (2014).
- [2] J. Lindl, *Phys Plasmas* **2**, 3933 (1995).
- [3] M. J. Edwards, P. K. Patel, J. D. Lindl, L. J. Atherton, S. H. Glenzer, S. W. Haan, J. D. Kilkenny, O. L. Landen, E. I. Moses, A. Nikroo, R. Petrasso, T. C. Sangster, P. T. Springer, S. Batha, R. Benedetti, L. Bernstein, R. Betti, D. L. Bleuel, T. R. Boehly, D. K. Bradley, J. A. Caggiano, D. A. Callahan, P. M. Celliers, C. J. Cerjan, K. C. Chen, D. S. Clark, G. W. Collins, E. L. Dewald, L. Divol, S. Dixit, T. Doeppner, D. H. Edgell, J. E. Fair, M. Farrell, R. J. Fortner, J. Frenje, M. G. Gatu Johnson, E. Giraldez, V. Y. Glebov, G. Grim, B. A. Hammel, A. V. Hamza, D. R. Harding, S. P. Hatchett, N. Hein, H. W. Herrmann, D. Hicks, D. E. Hinkel, M. Hoppe, W. W. Hsing, N. Izumi, B. Jacoby, O. S. Jones, D. Kalantar, R. Kauffman, J. L. Kline, J. P. Knauer, J. A. Koch, B. J. Kozioziemski, G. Kyrala, K. N. LaFortune, S. L. Pape, R. J. Leeper, R. Lerche, T. Ma, B. J. MacGowan, A. J. Mackinnon, A. MacPhee, E. R. Mapoles, M. M. Marinak, M. Mauldin, P. W. McKenty, M. Meezan, P. A. Michel, J. Milovich, J. D. Moody, M. Moran, D. H. Munro, C. L. Olson, K. Opachich, A. E. Pak, T. Parham, H. S. Park, J. E. Ralph, S. P. Regan, B. Remington, H. Rinderknecht, H. F. Robey, M. Rosen, S. Ross, J. D. Salmonson, J. Sater, D. H. Schneider, F. H. Seguin, S. M. Sepke, D. A. Shaughnessy, V. A. Smalyuk, B. K. Spears, C. Stoeckl, W. Stoeffl, L. Suter, C. A. Thomas, R. Tommasini, R. P. Town, S. V. Weber, P. J. Wegner, K. Widman, M. Wilke, D. C. Wilson, C. B. Yeamans, and A. Zylstra, *Phys Plasmas* **20**, 070501 (2013).
- [4] J. D. Kilkenny, P. Bell, R. Hanks, G. Power, R. E. Turner, and J. Wiedwald, *Rev Sci Instrum* **59**, 1793 (1988).
- [5] D. G. Hicks, N. B. Meezan, E. L. Dewald, A. J. Mackinnon, R. E. Olson, D. A. Callahan, T. Doppner, L. R. Benedetti, D. K. Bradley, P. M. Celliers, D. S. Clark, P. Di Nicola, S. N. Dixit, E. G. Dzenitis, J. E. Eggert, D. R. Farley, J. A. Frenje, S. M. Glenn, S. H. Glenzer, A. V. Hamza, R. F. Heeter, J. P. Holder, N. Izumi, D. H. Kalantar, S. F. Khan, J. L. Kline, J. J. Kroll, G. A. Kyrala, T. Ma, A. G. MacPhee, J. M. McNaney, J. D. Moody, M. J. Moran, B. R. Nathan, A. Nikroo, Y. P. Opachich, R. D. Petrasso, R. R. Prasad, J. E. Ralph, H. F. Robey, H. G. Rinderknecht, J. R. Rygg, J. D. Salmonson, M. B. Schneider, N. Simanovskaia, B. K. Spears, R. Tommasini, K. Widmann, A. B. Zylstra, G. W. Collins, O. L. Landen, J. D. Kilkenny, W. W. Hsing, B. J. MacGowan, L. J. Atherton, and M. J. Edwards, *Phys Plasmas* **19**, 122702 (2012).
- [6] J. Lindl, O. Landen, J. Edwards, E. Moses, and R. Tommasini, *Phys Plasmas* **21**, 020501 (2014).

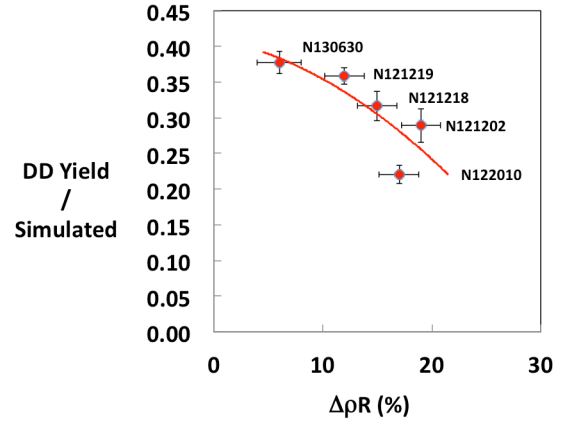


FIG. 7. The measured over expected yield ratio drops as the  $pR$  perturbations induced by tent increase in Low-Foot experiments. The plot shows a reduction in yield performance approaching factors of about 2x when the induced fractional perturbation  $\Delta(pR)/\Delta pR$  reaches the 20% value, i.e. for tent thicknesses in the 110nm range.



- [7] O. A. Hurricane, D. A. Callahan, D. T. Casey, P. M. Celliers, C. Cerjan, E. L. Dewald, T. R. Dittrich, T. Doppner, D. E. Hinkel, L. F. B. Hopkins, J. L. Kline, S. Le Pape, T. Ma, A. G. MacPhee, J. L. Milovich, A. Pak, H. S. Park, P. K. Patel, B. A. Remington, J. D. Salmonson, P. T. Springer, and R. Tommasini, *Nature* **1** (2014).
- [8] J. E. Field, J. R. Rygg, M. A. Barrios, L. R. Benedetti, T. Doppner, N. Izumi, O. Jones, S. F. Khan, T. Ma, S. R. Nagel, A. Pak, R. Tommasini, D. K. Bradley, and R. P. J. Town, *Rev Sci Instrum* **85**, 11 (2014).
- [9] K. M. Hanson, (1984).
- [10] S. R. Nagel and E. al, To Be Published **1** (2014).
- [11] T. R. Dittrich, O. A. Hurricane, D. A. Callahan, E. L. Dewald, T. Doppner, D. E. Hinkel, L. F. B. Hopkins, S. Le Pape, T. Ma, J. L. Milovich, J. C. Moreno, P. K. Patel, H. S. Park, B. A. Remington, J. D. Salmonson, and J. L. Kline, *Phys Rev Lett* **112**, (2014).
- [12] D. T. Casey, V. A. Smalyuk, K. S. Raman, J. L. Peterson, L. Berzak Hopkins, D. A. Callahan, D. S. Clark, E. L. Dewald, T. R. Dittrich, S. W. Haan, D. E. Hinkel, D. Hoover, O. A. Hurricane, J. J. Kroll, O. L. Landen, A. S. Moore, A. Nikroo, H. S. Park, B. A. Remington, H. F. Robey, J. R. Rygg, J. D. Salmonson, R. Tommasini, and K. Widmann, *Phys Rev E* **90**, 011102 (2014).
- [13] R. Tommasini and E. al, To Be Submitted (n.d.).
- [14] J. Gu, Z. Dai, Z. Fan, S. Zou, W. Ye, W. Pei, and S. Zhu, *Phys Plasmas* **21**, (2014).

---

<sup>i</sup> Electronic mail: [tommasini2@llnl.gov](mailto:tommasini2@llnl.gov)